Astrocytes phagocytose focal dystrophies from shortening myelin segments in the optic nerve of *Xenopus laevis* at metamorphosis

Elizabeth A. Mills[a], Chung-ha O. Davis[b], Eric A. Bushong[c], Daniela Boassa[c], Keun-Young Kim[c], Mark H. Ellisman[c,d], and Nicholas Marsh-Armstrong[a,b,1]

[a]The Solomon H. Snyder Department of Neuroscience, Johns Hopkins University School of Medicine, Baltimore, MD 21205; [b]Hugo W. Moser Research Institute at Kennedy Krieger, Inc., Baltimore, MD 21205; [c]National Center for Microscopy and Imaging Research, Center for Research in Biological Systems, University of California at San Diego, La Jolla, CA 92093; and [d]Department of Neurosciences, University of California at San Diego, La Jolla, CA 92093

Edited by Ben A. Barres, Stanford University School of Medicine, Stanford, CA, and approved June 29, 2015 (received for review April 1, 2015)

Oligodendrocytes can adapt to increases in axon diameter through the addition of membrane wraps to myelin segments. Here, we report that myelin segments can also decrease their length in response to optic nerve (ON) shortening during *Xenopus laevis* metamorphic remodeling. EM-based analyses revealed that myelin segment shortening is accomplished by focal myelin-axon detachments and protrusions from otherwise intact myelin segments. Astrocyte processes remove these focal myelin dystrophies using known phagocytic machinery, including the opsonin milk fat globule-EGF factor 8 (Mfge8) and the downstream effector ras-related C3 botulinum toxin substrate 1 (Rac1). By the end of metamorphic nerve shortening, one-quarter of all myelin in the ON is enwrapped or internalized by astrocytes. As opposed to the removal of degenerating myelin by macrophages, which is usually associated with axonal pathologies, astrocytes selectively remove large amounts of myelin without damaging axons during this developmental remodeling event.

thyroid hormone | glia | lipid droplet | *Mfge8*

Myelin exists as regularly spaced segments that enable fast and efficient transfer of information across long distances through saltatory propagation of action potentials between nodes of Ranvier (1). The number, length, and thickness of individual segments vary with species and nervous system region (2). The proper thickness and length of myelin segments are likely established, at least in part, during the myelination process itself, which involves the dynamic elongation, shortening, and removal of individual segments (3, 4). However, once established, some myelin segments must be modified further to accommodate axonal growth. Developmental increases in axon diameter are coupled to the addition of membrane wraps to myelin segments, thereby maintaining a near-linear relationship between axon caliber and myelin thickness (5, 6). In the peripheral nervous system, Schwann cell myelin segments can also elongate in proportion to nerve length, increasing internodal distances by as much as a factor of four (3, 7). The regulation of myelin on axons is essential for the proper function of the vertebrate nervous system, because both hypomyelination and hypermyelination lead to neuropathy (8). However, the mechanisms involved in myelin segment plasticity have remained poorly understood, in part, because of the difficulty in studying a process that occurs in mammals during a protracted period as the animals mature (2).

During metamorphic remodeling of the head in *Xenopus laevis*, the optic nerve (ON) and its associated axons rapidly shorten in length (9). A description of this process (10) noted abnormally folded myelin on axons and membranous material inside glial cells, suggesting that myelin might be remodeling, thereby providing a model system in which to study myelin plasticity. The current study set out to determine how myelin segments remodel during ON shortening.

Results

The ON and Its Myelinated Axons Widen and Shorten During *X. laevis* Metamorphosis. The head of the vertebrate *X. laevis* becomes smaller and more triangular between Nieuwkoop and Faber (NF) (11) stage 58, just before metamorphic climax, and the completion of metamorphosis at stage 66 (Fig. 1*A*), over the course of approximately 1 wk. Measurements in dissected ONs confirmed previous studies (9), showing that the ON decreased in length by approximately one-half (Fig. 1*B*), whereas the cross-sectional area doubled in thickness (Fig. 1*C*). However, because the increase in thickness is transient, only at the climax of metamorphosis (Fig. 1*C*), the ON ultimately experiences a net loss of volume.

ON cross-sections immunolabeled for brain lipid-binding protein (Blbp, also known as Fabp7), an astrocyte lineage marker (12), and acetylated α-tubulin, an axon marker, showed a similar architecture at all stages (Fig. S1*A*), with radially arranged astrocytes with pial-attached end feet, similar to the rodent ON head (13). Unlike mammals, where nearly all ON axons are myelinated (14), less than 10% of axons are myelinated in the ON of *X. laevis* (15). Importantly, the colocalization of myelin basic protein (Mbp) with the degenerating axon marker cleaved caspase-3 (16) demonstrated no specific loss of myelinated axons at metamorphosis (Fig. S1 *B*–*G*).

To determine how ON myelinated axons remodel at metamorphosis, transmission electron microscopy (TEM) micrographs were taken from the center of ONs (Fig. S1*H*), the region of the most dynamic shortening (10), and myelin and enclosed axons were traced (Fig. 1*E*). Similar to the ON as a whole, the axolemma of individual myelinated axons undergoes a transient doubling in

Significance

Myelin segments facilitate fast conduction along axons, and thus the rapid transmission of information in the nervous system. In the absence of pathology, myelin segments are generally regarded as highly stable structures with plasticity limited to growth-related increases in myelin thickness. We discovered that existing myelin segments are also capable of rapid shortening and demonstrate that shortening involves a characteristic focal dystrophy that develops at the contact point with a phagocytic astrocyte. These astrocytes internalize large quantities of myelin from shortening segments using known phagocytic machinery in a developmentally regulated manner. This mechanism likely contributes to other instances of myelin remodeling and prevents the persistence of potentially pathological myelin dystrophies.

Author contributions: E.A.M. and N.M.-A. designed research; E.A.M., C.-h.O.D., E.A.B., D.B., and K.-Y.K. performed research; M.H.E. contributed new reagents/analytic tools; E.A.M. and N.M.-A. analyzed data; and E.A.M. and N.M.-A. wrote the paper.

The authors declare no conflict of interest.

This article is a PNAS Direct Submission.

Freely available online through the PNAS open access option.

[1]To whom correspondence should be addressed. Email: marsh-armstrong@jhmi.edu.

This article contains supporting information online at www.pnas.org/lookup/suppl/doi:10.1073/pnas.1506486112/-/DCSupplemental.

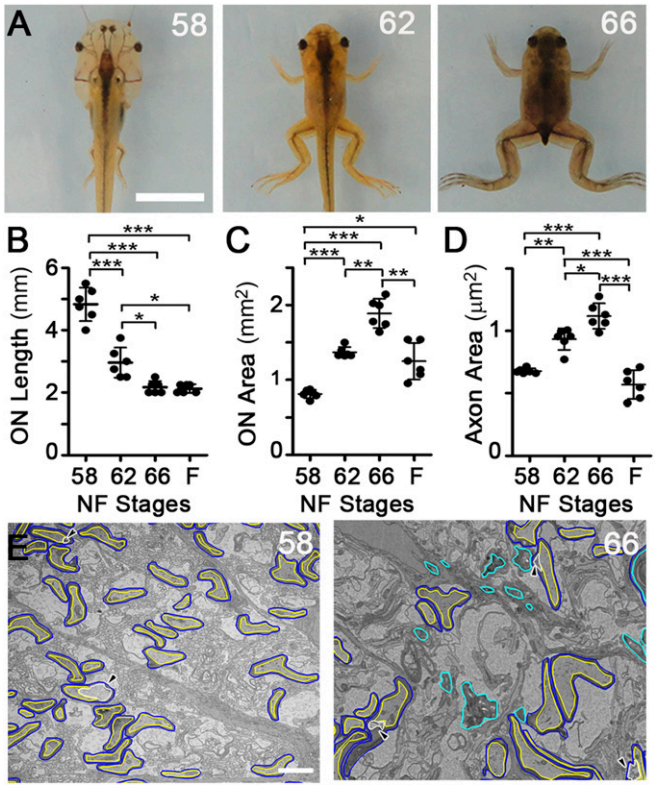

Fig. 1. The ON and its myelinated axons both shorten and transiently widen at metamorphosis. (*A*) Head remodeling in *X. laevis* at premetamorphic NF stage 58, metamorphic climax stage 62, and immediately postmetamorphic climax stage 66. (Scale bar: 1 cm.) ON length (*B*) and cross-sectional area (*C*) during metamorphosis. F, juvenile frogs 4 wk postmetamorphosis. (*D*) Myelinated axon axoplasm cross-sectional area, averaged per ON. Values derive from 6,975, 5,759, 5,267, and 6,076 axons at stages 58, 62, and 66 and in F, respectively. (*E*) Representative traced TEM micrographs of the ON cross-sections at stages 58 and 66. Myelin sheaths (blue), axoplasm (yellow), focal periaxonal space enlargements (white and arrowheads), and myelin not associated with axons (cyan) are illustrated. (Scale bar: 2 μm.) Mean ± SD is shown (n = 6 ON per stage). *P < 0.05; **P < 0.01; ***P < 0.001 (by the Games–Howell test).

cross-sectional area and a subsequent decrease back to premetamorphic size within 1 mo (Fig. 1*D*), demonstrating that the axons remodel in concordance with the ON as a whole.

Extensive Myelin Is Removed from Segments During Metamorphosis. Counts of myelinated axons in TEM micrographs of ON cross-sections (Fig. S2*A*) confirmed that ON shortening did not interfere with the normal addition of new myelinated axons, known to occur throughout the lifespan of *X. laevis* (17), or with the continued addition of myelinating oligodendrocytes in the ON during this time (Fig. S2*B*). To determine whether there was a change in the relationship between myelin and axons during ON shortening, we used the G′-ratio, a modification of the G-ratio (18), as a measure of myelin thickness per axon (*Materials and Methods*). The G′-ratio distribution remained constant during metamorphosis and only shifted toward thicker myelin in the juvenile frogs (Fig. S2*C*), consistent with the increase in retinal ganglion cell axon conduction velocity observed in frogs relative to tadpoles (19). The increased myelin per axon after metamorphosis was also reflected in the ratio of myelin area to axoplasm area (Fig. 2*A*). Interestingly, unlike the G′-ratio, there was a trend toward an elevated myelin-to-axoplasm ratio already at the end of metamorphic climax. Further TEM analyses explained the difference between these two metrics, because there was a disruption in the relationship between myelin and axons specifically during ON shortening. First, there was a marked increase in focal detachments between the innermost myelin membrane and the axonal membrane, leading to focal enlargements of periaxonal space per ON cross-section, from 20.8 ± 6.9 μm^2 at

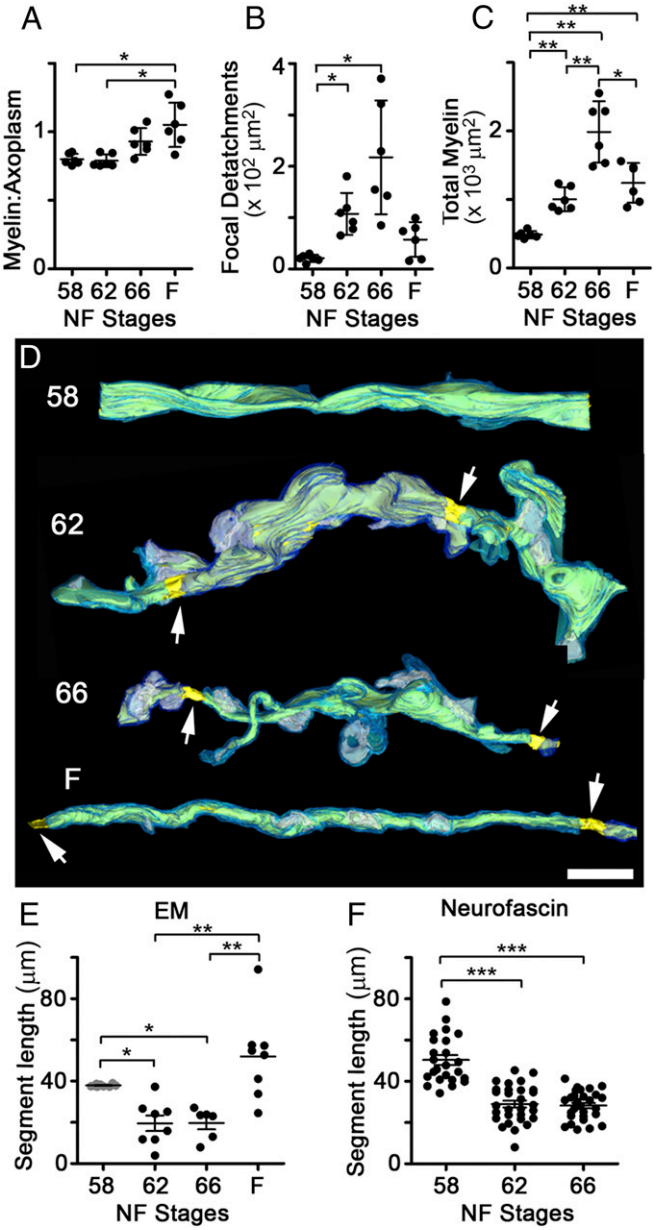

Fig. 2. Myelin segment shortening involves an alteration of the myelin-axon relationship. (*A*) Mean ratio of myelin area over axoplasm area per axon, averaged per ON. (*B*) Total cross-sectional area of periaxonal spaces under focal myelin detachments, per ON. (*C*) Total area of myelin, per ON cross-section. (*D*) Reconstructions of axons at stages 58, 62, and 66 and in F, based on SBEM datasets datasets and shown over black backgrounds, with traced myelin (light and dark blue), axoplasm (yellow), focal periaxonal space enlargements (white), and nodes of Ranvier (arrows). (Scale bar: 5 μm.) (Additional axons are shown in Fig. S2*D*). (*E*) Internodal distances measured from SBEM-traced axons. Stage 58 values (gray) are minimum lengths because segments generally exceeded the volume dimensions (n = 10, 8, 6, and 8 segments at stages 58, 62, and 66 and in F, respectively). (*F*) Internodal distances (n = 23, 28, and 28 axons at stages 58, 62, and 66; n = 3 ONs per stage) measured in ON volumes immunolabeled with 3A10 and neurofascin. In *A*–*C*, measurements are from traced TEM micrographs (n = 6). Mean ± SD is shown. *P < 0.5; **P < 0.01; ***P < 0.001 [by the Games–Howell (*A*–*C*), Kruskal–Wallis (*E*), and Tukey's (*F*) tests].

stage 58 to 217 ± 111 μm^2 at stage 66 (Fig. 2*B*). Second, even though the amount of myelin on axons was greatest in juvenile frogs (Fig. S2 *A* and *C*), the total area of myelin within the ON was highest at stage 66 (Fig. 2*C*), suggesting that there might be large amounts of myelin not associated with axons at the completion of metamorphosis.

Serial block-face scanning electron microscopy (SBEM) analyses (Fig. 2*D* and Fig. S2*D*) revealed prominent outpocketings of myelin specifically at metamorphic climax, which, along with nearby focal myelin-axon detachments, could be indicative of rapid segment shortening. Indeed, tracing the distance between nodes in the reconstructed SBEM volumes revealed that the internodal distance approximately halved at metamorphosis, from greater than 38.0 ± 0.6 μm at stage 58 (an underestimation) to 19.7 ± 7.9 μm at stage 66 (Fig. 2*E*). The shortening of myelin segments was confirmed in ON confocal image stacks immunolabeled for the myelinated axon marker 3A10 (Fig. S1 *B–D*) and the paranodal marker neurofascin (Fig. 2*F* and Fig. S2*E*).

Myelin Is Found Outside Axons and Within Phagocytes at Metamorphosis. Tracing of cellular processes adjoining myelin segments in a subset of axons (Fig. S3*A*) demonstrated that the myelin protrusions extending from axons were contacted and enwrapped by the processes of neighboring cells. These reconstructions also helped to explain the diversity of myelin profiles observed in the TEM analyses (Fig. 3*A*), which included whorls of myelin still connected to axons, myelin enwrapped by lamellar processes, and myelin contained within cells at advanced states of degradation. The tracing of an ON phagocyte from a stage 62 SBEM volume (Fig. 3*B*) shows a phagocyte enwrapping a focal myelin protrusion with multiple lamellar processes, and also containing within its cytoplasm the remnants of another internalized myelin fragment in the early stages of breakdown. This and similar reconstructions (Fig. S3*A*) demonstrate that myelin segment shortening occurs through the removal of myelin from intact individual myelin segments through the selective phagocytosis of small focal intrasegmental myelin dystrophies.

The total area of debris myelin per ON cross-section increased more than 50-fold, from 7 ± 4 μm^2 at stage 58 to 492 ± 247 μm^2 at stage 66 (Fig. 3*C*). As a result, approximately one-quarter (24.3 ± 8.8%) of all myelin in the ON at the end of metamorphosis, stage 66, was classified as debris (Fig. 3*D*). Finding large amounts of myelin outside axons was confirmed by immunohistochemistry (Fig. S3 *B* and *C*), although the percentage was much lower, possibly due to myelin losing antigenicity after phagocytosis. In EM, the internalized myelin appears to coalesce within the phagocytes, because the size of debris myelin significantly increased from 0.5 ± 0.2 μm^2 at stage 58 to 1.2 ± 0.1 μm^2 at stage 66 (Fig. 3*E*). Larger groupings of debris were often localized near lipid droplets (Fig. S3 *D* and *E*), suggesting that ON phagocytes internalize large amounts of myelin and metabolize at least a fraction of it.

Astrocytes Are the Primary Myelin Phagocytes During ON Shortening. The clearance of myelin debris in the nervous system, as occurs during injury or disease, is usually associated with monocyte recruitment and inflammation (20). Consistent with the results of others demonstrating a lack of monocytes in the frog ON in the absence of injury (10, 21), the density of *Bandeiraea simplicifolia (Griffonia simplicifolia)* isolectin B4 (IB4)–positive microglia (Fig. 4*A*) within the ON parenchyma remained constant during metamorphosis (Fig. 4*B*), while increasing nearly fourfold only in the ON sheath (Fig. 4*C*). This lack of infiltration did not represent an inability of microglia to infiltrate and clear debris during metamorphosis, because there was an approximately fourfold increase in IB4-lectin–positive microglia within the ON parenchyma 3 d after a unilateral ON transection (Fig. S4 *A* and *B*). Astrocytes, on the other hand, exhibited characteristics associated with phagocytosis during metamorphosis. ON astrocytes experienced significant increases in lysosomes and lipid droplets, as evident by *Blbp* promoter-driven transgenic reporters for late lysosomes and lipid droplets, Cd63-mCherry and Mettl7b-mCherry (22), respectively (Fig. S4 *C–F*). Together with the finding that ON astrocytes express (Fig. 4*D* and Fig. S4*H*) and may up-regulate (Fig. S4*G*) genes involved in phagocytosis at metamorphosis (23), including low density lipoprotein receptor-related protein 1 (*lrp1*), *mfge8*, and *rac1*, these data suggested that removal of myelin debris at metamorphosis is a developmental event that might involve astrocytes as the primary phagocytes.

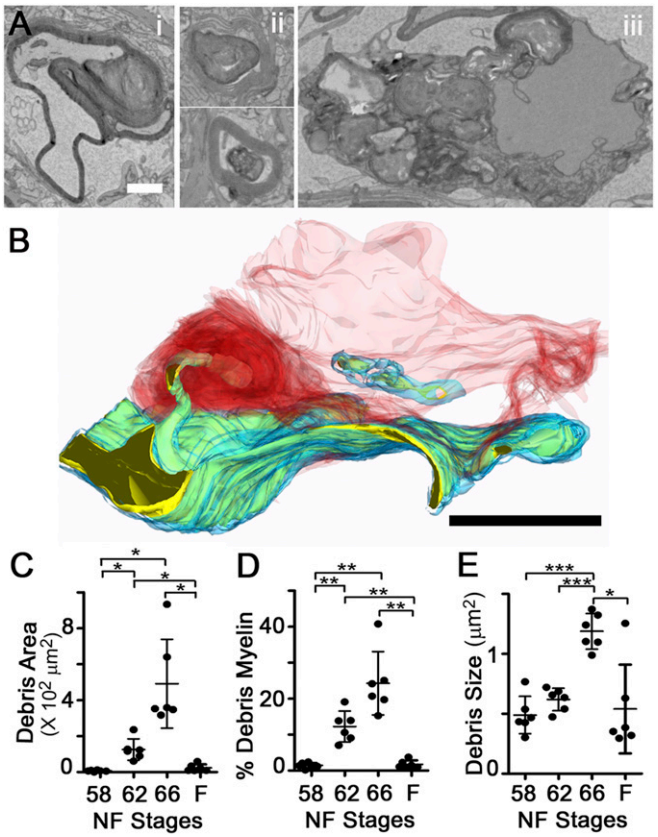

Fig. 3. Large fraction of myelin at metamorphosis is debris. (*A*) Debris myelin intermediates in TEM micrographs from stage 66 ON cross-sections include myelin whorls associated with axons (*i*) and debris myelin enwrapped by phagocyte lamellar processes (*ii*) or within phagocyte soma (*iii*). (Scale bar: 1 μm.) (*B*) SBEM-based reconstruction shows a phagocyte (red) using lamellar processes (dark red) to internalize axonal material containing both myelin (blue) and axoplasm (yellow). (Scale bar: 5 μm.) (Additional axons are illustrated in Fig. S3*C*). (*C*) Total area of debris myelin per ON cross-section. (*D*) Percentage of all myelin in the form of debris, per ON cross-section. (*E*) Mean area of individual debris myelin fragments, per ON cross-section. In *C–E*, measurements are from traced TEM micrographs. Mean ± SD is shown (n = 6 ONs). *P < 0.05; **P < 0.01; ***P < 0.001 (by the Games–Howell test).

Because transformations during *X. laevis* metamorphosis are under transcriptional control of a surge of circulating thyroid hormone (TH) (24), cell type-specific expression of a TH receptor dominant negative construct in which the C-terminal transactivation domain (TRΔC) is deleted (25, 26) was used to test whether TH regulated the phagocytic removal of focal myelin dystrophies from shortening segments during metamorphosis. The transgenic expression of TRΔC in astrocytes through the *Blbp* promoter, sufficient in a TH-induction assay to reduce TH-mediated gene expression in ON astrocytes (Fig. S5 *A–C*), led to an elevation in the ratio of myelin to axoplasm and the amount of myelin detachments on axons at stage 66 (Fig. 4 *E* and *F*), which are signs of myelin not being properly removed. In contrast, TRΔC expression in oligodendrocytes, under the *Mbp* promoter, trended toward having smaller myelin detachments, which is likely due to lower overall myelin levels (Fig. S5*D*), suggesting

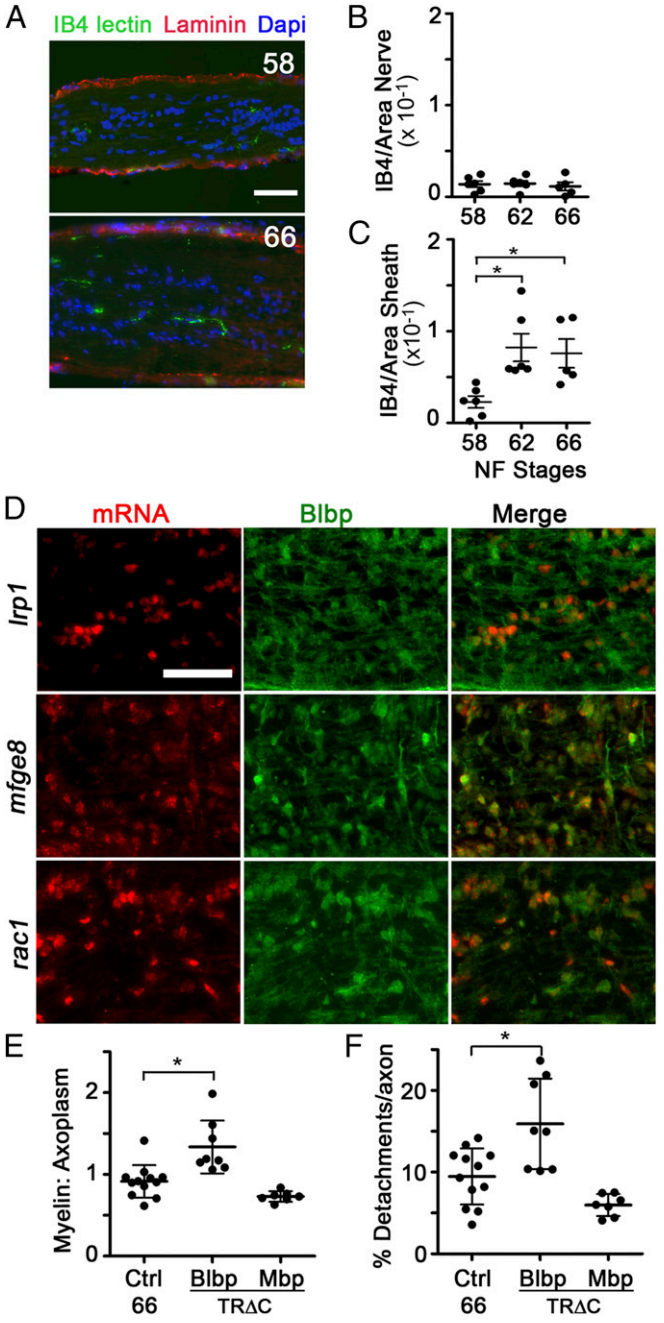

Fig. 4. Astrocytes are the primary phagocytes at metamorphosis. (*A*) Microglia, labeled by IB4-lectin-FITC (IB4 lectin, green), found in the ON parenchyma and laminin-immunolabeled ON sheath (red) at stages 58 and 66. Nuclei are labeled with DAPI (blue). (Scale bar: 50 μm.) IB4 signal per unit area in ON parenchyma (*B*) and ON sheath (*C*) is shown. (*D*) Astrocytes, immunolabeled with Blbp (green), express mRNAs (red) for phagocytic genes *lrp1*, *mfge8*, *rac1*, and many others (Fig. S4C), shown at stage 62. (Scale bar: 50 μm.) In *B* and *C*, the IB4 signal per unit area in individual ONs ($n = 5$) is shown with the mean ± SD. $^*P < 0.05$ by Tukey's test. (*E*) Myelin/axoplasm ratio per axon averaged per ON at stage 66. (*F*) Percentage of axon area that represents focal myelin detachments per axon at stage 66 ($n = 12$ control and $n = 8$ TRΔC in *E* and *F*). Values derive from 5,418, 3,014, and 3,450 axons in the control, Blbp:TRΔC, and Mbp:TRΔC groups, respectively.

that the TH-dependent myelin removal function is specific to astrocytes.

To determine whether astrocytes were using their phagocytic machinery to remove myelin debris, we chose to target both the downstream effector GTPase Rac1 and the Mfge8-integrin receptor system. The dominant negative Rac1N17 (27), which sequesters Rac-activating guanine nucleotide exchange factors (28), was driven in astrocytes by the *Blbp* promoter in a tetracycline-inducible manner, beginning at stage 58. The percentage of debris myelin surrounded by lamellar processes in stage 62 Rac1N17 ONs was decreased to 4.4 ± 5.3% compared with 14.1 ± 7.8% in control ONs (Fig. 5*A*), suggesting an impairment in lamellar process formation or motility. Furthermore, the percentage of the axon area containing focal myelin detachments and the ratio of myelin to axoplasm were also significantly increased in Rac1N17 ONs at stage 66 (Fig. 5 *B* and *C*). Therefore, the impairment of a key phagocytic effector in astrocytes at metamorphosis led to a phenotype highly similar to the phenotype observed after inhibiting TH action specifically in astrocytes, further supporting the notion that ON astrocytes are the primary phagocytes of focal myelin dystrophy removal at metamorphosis.

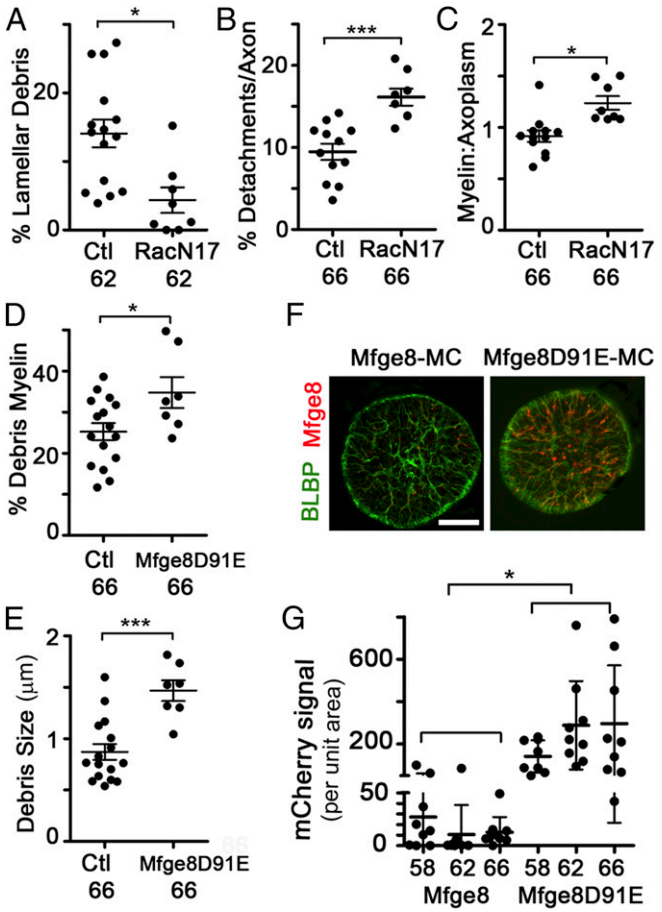

Fig. 5. Astrocyte expression of *Rac1* or *Mfge8* dominant negative transgenes inhibit discrete aspects of myelin phagocytosis. (*A*) Percentage of debris myelin enwrapped by lamellar processes at stage 62 per ON. (*B*) Percentage of axon area that represents focal myelin detachments per axon at stage 66, per ON. (*C*) Myelin/axoplasm ratio per axon per ON at stage 66. (*D*) Percentage of debris myelin by area per ON at stage 66. (*E*) Mean size of individual debris myelin units per ON at stage 66. (*F*) Immunofluorescence due to *Tg(Blbp:Mfge8-mCherry)* transgene or *Tg(Blbp:Mfge8D91EmCherry)* transgene in ON cross-sections at stage 66. (Scale bar: 50 μm.) (*G*) mCherry signal per unit area is elevated in the Mfge8D91E-mCherry transgene relative to the Mfge8-mCherry transgene at all stages. In *A*–*D*, measurements are from traced TEM micrographs. Mean ± SD is shown ($n = 16$ control and $n = 8$ transgenic in *A*, *D*, and *E*; $n = 12$ control and $n = 8$ transgenic in *B* and *C*). $^*P < 0.05$; $^{***}P < 0.001$ [by Dunnett's test (*A*, *D*, and *E*) or the Games–Howell test (*B*, *C*, and *G*)].

We also examined the effect of Mfge8 in metamorphic ON shortening, because Mfge8 opsinization is one of several pathways used by phagocytes to clear cell debris (29). Expression in astrocytes of Mfge8-D91E, which acts in a dominant negative manner (29) because it binds debris membranes with exposed phosphatidylserine but not the integrin receptors on the phagocytes, leads to an increase in the percentage of debris myelin in the ON at stage 66, from its already high levels of 25.3 ± 8.3% in control animals to 34.8 ± 7.6% in Mfge8-D91E animals (Fig. 5*D*). The size of the debris myelin also nearly doubled, from 0.88 μm^2 in control ONs to 1.47 μm^2 in Mfge8-D91E ONs (Fig. 5*E*). These results suggest that Mfge8 is critical for the efficient degradation and clearance of myelin from astrocytes following its internalization.

The localization of Mfge8-tagged debris was also visualized using the mCherry tag as a reporter, because mCherry maintains fluorescence within acidified compartments (30). In ON cross-sections, mCherry-labeled puncta were detected within astrocyte processes, especially the astrocyte end feet at the ON sheath pial lining (Fig. 5*F*). The size and intensity of the mCherry-labeled puncta were larger in the ONs of animals expressing the Mfge8-D91E transgene (Fig. 5 *F* and *G*), suggesting that Mfge8 only transiently associates with debris, but that in the absence of integrin binding, this association is prolonged and debris accumulates within the astrocyte. These data further support the model, proposed in other systems (31), that the primary role for Mfge8 is in facilitating degradation rather than internalization. Together with the TRΔC and Rac1N17 data, as well as the SBEM data, these experiments demonstrate that astrocytes are principally responsible for the removal of focal myelin dystrophies from intact myelin segments during metamorphic myelin segment shortening.

Discussion

This work demonstrates that in a developing vertebrate ON, individual myelin segments can shorten in response to decreases in axon length, revealing a plasticity of myelin segments not previously known. Through EM-based quantifications, we demonstrate that axon myelin segments shorten through selective astrocytic phagocytosis of small focal intrasegmental myelin dystrophies. This mechanism may be relevant to the homeostatic maintenance of myelin segments or in other instances where myelin segment length may need to be modified, such as the maintenance of myelin boundaries in transition zones, the accommodation of new segments replacing damaged ones during normal myelin turnover (32), aging (33), or regeneration (34). Although replacement segments generally start out short during regeneration, they can elongate to a length consistent with the other segments on their associated axon (34), requiring the simultaneous shortening of neighboring segments. Furthermore, this process may be involved in the removal of focal regions of excess myelin that have been found on rodent ON axons during early myelination and subsequently resolved via an unknown mechanism (35).

The prominent detachments within myelin segments that focally separated axon and myelin membranes, as well as protrusions extending from the myelin sheath observed during metamorphosis, are indicative of a breakdown in axoglial interactions (36), likely due to the distortion of the myelin sheath as the axon becomes shorter and wider. Because adhesive attachments between myelin and axonal membranes are stronger at paranodal than internodal regions (37), axon remodeling would be expected to disrupt axoglial attachments preferentially at internodal regions, as we observed.

Our knowledge of the roles played by astrocytes has expanded following the discovery that they express phagocytic machinery (23). To date, a role for astrocytes in the clearance of myelin has only been appreciated in pathological contexts (38, 39). Here, we provide evidence that ON astrocytes can also clear much myelin in a developmentally regulated nonpathological manner, because the extensive focal dystrophies within individual segments were not accompanied by either axon loss or visible defects in myelin lamellae compaction. The continual removal of small regions of dystrophic myelin from intact axons could provide a homeostatic mechanism to prevent the large-scale loss of myelin and fragmentation of axons that triggers a pathological immune response. We confirmed earlier reports that monocytes do not infiltrate the ON at metamorphosis, although a contribution to myelin clearance by the small amount of resident microglia cannot be ruled out. We also demonstrated that the focal myelin protrusions are enwrapped and phagocytized by astrocytes. Of particular note is the formation of lamellar wraps by astrocyte processes around myelin protrusions, because these structures were specifically affected by inhibiting Rac1-dependent actin remodeling within astrocytes. Although inhibition of the integrin-Mfge8 phagocytic receptor system produced myelin debris clearance deficits, other receptor systems are likely also involved in myelin phagocytosis. Megf10 and MertK have been shown to play prominent roles in phagocytic remodeling of the visual system during mouse development (40). Indeed, due to its roles in lipid metabolism (41) and myelin internalization in demyelinating diseases (42), the ced-1 homolog Lrp1 may also be involved.

The persistence of regions of excess myelin can lead to neurodegeneration, and debris myelin is known to provoke inflammation (43, 44). Basal astrocyte phagocytic activity may be a principal mechanism regulating the CNS response to excess myelin and debris buildup under homeostatic conditions. By the end of metamorphosis, one-quarter of all myelin was in the form of debris associated with astrocytes, likely reflecting more than the astrocytes' high internalization capacities but also their slow degradation abilities. Indeed, the fluorescence pattern of the Mfge8-mCherry transgenes was indicative that some debris myelin was processed within astrocytes but then transported to the pial surface of the frog ON, suggesting that astrocytes may pass some of the debris to professional phagocytes, possibly explaining the increase of monocytes in the sheath during metamorphic climax. Because the frog ON is not internally vascularized, this sheath is the equivalent of the recently described perivascular spaces of mammals, where large amounts of debris and metabolites are flushed daily from the brain (45).

Materials and Methods

Animals and Transgenes. WT *X. laevis* were obtained from Xenopus Express. Transgenic *X. laevis* were generated via restriction enzyme mediated integration (REMI) transgenesis (46) and bred to WT animals. All animal experiments were carried out in accordance with procedures approved by the Institutional Animal Care and Use Committee of Johns Hopkins University School of Medicine. The dominant negative TH receptor construct (TRΔC), based on a study by Marsh-Armstrong et al. (26), was expressed in astrocytes or oligodendrocytes through a tetracycline operator (47) in combination with the tetracycline reverse transactivator rtTA2 (47) driven by the *Xenopus tropicalis Blbp* (48) or mouse *Mbp* (49) promoter, inducing transgene expression with doxycycline starting at stage 58. *X. tropicalis* Rac1N17 was also expressed conditionally using *Tg(Blbp:rtTA2)*. *X. tropicalis* Mfge8 was expressed through the *Blbp* promoter. Transgenic controls expressed membrane versions of mCherry [with tags from *X. laevis* Gap43 or human Mettl7b (22)] driven by the *Blbp* and zebrafish *Islet2* (50) promoters, respectively.

EM and EM-Based Quantifications. EM processing was carried out as previously described (51). For the initial characterization, ONs from six WT *X. laevis* each at NF stages 58, 62, and 66 and at 4 wk postmetamorphosis were used. For the transgenic perturbation studies, four animals each at stage 62 and stage 66 for each transgene, including the two transgenic controls, were used. Most ONs were sectioned in a cross-sectional orientation, and 10 generally nonoverlapping images spanning all areas of the ON were imaged at a magnification of 5,000× with an H7600 (Hitachi) transmission electron microscope. Manual tracing of the axoplasm, outer myelin sheath, focal periaxonal space, and debris myelin was carried out for 10 micrographs per ON in a blinded fashion, and images were quantified using IPlab software (Becton Dickinson) custom scripts. To extrapolate the myelin inner diameter for the calculation of G′-ratios, the areas of the axoplasm and periaxonal spaces were subtracted from the area bounded by the myelin sheath for each axon. For the measurements of myelin area, myelin was automatically segmented using IPlab software based on myelin being the most electron-dense structure in the

micrographs. For SBEM imaging, longitudinal sections were imaged on an FEI Quanta 200 (stage 62), Zeiss Sigma (stages 58 and 66), or Zeiss Merlin (juvenile frog) scanning electron microscope equipped with a Gatan 3View unit. Axons were traced using IMOD software (52), and internodal length was measured using Imaris software (Bitplane).

Immunohistochemistry, Image Quantification, and Statistical Analyses. In situ hybridization and immunohistochemistry were carried out on cryosections as previously described (48). Statistical analyses involved the comparison of means using *t* tests or single-variable ANOVAs using Graphpad Prism software and Brightstat (53). All graphs depict the mean ± SD. Statistical significance was defined as $P < 0.05$. Analyses are described in detail in *SI Materials and Methods*.

ACKNOWLEDGMENTS. We thank the Johns Hopkins University School of Medicine Neuroscience Imaging (NS050274) and Wilmer Eye Institute Microscopy (P30-EY001865) cores, Peter Brophy for the neurofascin NFC2 antibody, and Judy V. Nguyen for pCS2:Cd63-mCherry. This work was supported by Grant R01 EY019960 and a Catalyst for a Cure grant from the Glaucoma Research Foundation (to N.M.-A.). This work was also supported by National Center for Research Resources Grant 5P41RR004050, National Institute on Drug Abuse Human Brain Project Grant DA016602, and National Institute of General Medical Sciences Grants 5R01GM82949 and 5P41GM103412 (to M.H.E.).

1. Huxley AF, Stampfli R (1949) Evidence for saltatory conduction in peripheral myelinated nerve fibres. *J Physiol* 108(3):315–339.
2. Baumann N, Pham-Dinh D (2001) Biology of oligodendrocyte and myelin in the mammalian central nervous system. *Physiol Rev* 81(2):871–927.
3. Fried K, Hildebrand C, Erdélyi G (1982) Myelin sheath thickness and internodal length of nerve fibres in the developing feline inferior alveolar nerve. *J Neurol Sci* 54(1): 47–57.
4. Liu P, Du JL, He C (2013) Developmental pruning of early-stage myelin segments during CNS myelination in vivo. *Cell Res* 23(7):962–964.
5. Friede RL, Miyagishi T (1972) Adjustment of the myelin sheath to changes in axon caliber. *Anat Rec* 172(1):1–14.
6. Berthold CH, Nilsson I, Rydmark M (1983) Axon diameter and myelin sheath thickness in nerve fibres of the ventral spinal root of the seventh lumbar nerve of the adult and developing cat. *J Anat* 136(Pt 3):483–508.
7. Court FA, et al. (2004) Restricted growth of Schwann cells lacking Cajal bands slows conduction in myelinated nerves. *Nature* 431(7005):191–195.
8. Suter U, Scherer SS (2003) Disease mechanisms in inherited neuropathies. *Nat Rev Neurosci* 4(9):714–726.
9. Cullen MJ, Webster HD (1979) Remodelling of optic nerve myelin sheaths and axons during metamorphosis in Xenopus laevis. *J Comp Neurol* 184(2):353–362.
10. Cima C, Grant P (1982) Development of the optic nerve in Xenopus laevis. II. Gliogenesis, myelination and metamorphic remodelling. *J Embryol Exp Morphol* 72:251–267.
11. Nieuwkoop PD, Faber J, eds (1956) *Normal Table of Xenopus laevis (Daudin). A Systematical and Chronological Survey of the Development from the Fertilized Egg Until the End of Metamorphosis* (North-Holland, Amsterdam).
12. Schmid RS, Yokota Y, Anton ES (2006) Generation and characterization of brain lipid-binding protein promoter-based transgenic mouse models for the study of radial glia. *Glia* 53(4):345–351.
13. Sun D, Lye-Barthel M, Masland RH, Jakobs TC (2009) The morphology and spatial arrangement of astrocytes in the optic nerve head of the mouse. *J Comp Neurol* 516(1): 1–19.
14. Forrester J, Peters A (1967) Nerve fibres in optic nerve of rat. *Nature* 214(5085): 245–247.
15. Gaze RM, Peters A (1961) The development, structure and composition of the optic nerve of Xenopus laevis (Daudin). *Q J Exp Physiol Cogn Med Sci* 46:299–309.
16. Schoenmann Z, et al. (2010) Axonal degeneration is regulated by the apoptotic machinery or a NAD+-sensitive pathway in insects and mammals. *J Neurosci* 30(18): 6375–6386.
17. Wilson MA (1971) Optic nerve fibre counts and retinal ganglion cell counts during development of Xenopus laevis (Daudin). *Q J Exp Physiol Cogn Med Sci* 56(2):83–91.
18. Rushton WA (1951) A theory of the effects of fibre size in medullated nerve. *J Physiol* 115(1):101–122.
19. Chung SH, Stirling RV, Gaze RM (1975) The structural and functional development of the retina in larval Xenopus. *J Embryol Exp Morphol* 33(4):915–940.
20. Stoll G, Jander S (1999) The role of microglia and macrophages in the pathophysiology of the CNS. *Prog Neurobiol* 58(3):233–247.
21. Goodbrand IA, Gaze RM (1991) Microglia in tadpoles of Xenopus laevis: Normal distribution and the response to optic nerve injury. *Anat Embryol (Berl)* 184(1):71–82.
22. Zehmer JK, Bartz R, Liu P, Anderson RG (2008) Identification of a novel N-terminal hydrophobic sequence that targets proteins to lipid droplets. *J Cell Sci* 121(Pt 11): 1852–1860.
23. Cahoy JD, et al. (2008) A transcriptome database for astrocytes, neurons, and oligodendrocytes: A new resource for understanding brain development and function. *J Neurosci* 28(1):264–278.
24. Shi YB, Wong J, Puzianowska-Kuznicka M (1996) Thyroid Hormone Receptors: Mechanisms of Transcriptional Regulation and Roles during Frog Development. *J Biomed Sci* 3(5):307–318.
25. Schreiber AM, Das B, Huang H, Marsh-Armstrong N, Brown DD (2001) Diverse developmental programs of Xenopus laevis metamorphosis are inhibited by a dominant negative thyroid hormone receptor. *Proc Natl Acad Sci USA* 98(19):10739–10744.
26. Marsh-Armstrong N, Huang H, Remo BF, Liu TT, Brown DD (1999) Asymmetric growth and development of the Xenopus laevis retina during metamorphosis is controlled by type III deiodinase. *Neuron* 24(4):871–878.
27. Feig LA, Cooper GM (1988) Relationship among guanine nucleotide exchange, GTP hydrolysis, and transforming potential of mutated ras proteins. *Mol Cell Biol* 8(6): 2472–2478.
28. Schweighoffer F, et al. (1993) Identification of a human guanine nucleotide-releasing factor (H-GRF55) specific for Ras proteins. *Oncogene* 8(6):1477–1485.
29. Hanayama R, et al. (2002) Identification of a factor that links apoptotic cells to phagocytes. *Nature* 417(6885):182–187.
30. Shaner NC, et al. (2004) Improved monomeric red, orange and yellow fluorescent proteins derived from Discosoma sp. red fluorescent protein. *Nat Biotechnol* 22(12): 1567–1572.
31. Peng Y, Elkon KB (2011) Autoimmunity in MFG-E8-deficient mice is associated with altered trafficking and enhanced cross-presentation of apoptotic cell antigens. *J Clin Invest* 121(6):2221–2241.
32. Young KM, et al. (2013) Oligodendrocyte dynamics in the healthy adult CNS: Evidence for myelin remodeling. *Neuron* 77(5):873–885.
33. Lasiene J, Matsui A, Sawa Y, Wong F, Horner PJ (2009) Age-related myelin dynamics revealed by increased oligodendrogenesis and short internodes. *Aging Cell* 8(2): 201–213.
34. Powers BE, et al. (2013) Remyelination reporter reveals prolonged refinement of spontaneously regenerated myelin. *Proc Natl Acad Sci USA* 110(10):4075–4080.
35. Snaidero N, et al. (2014) Myelin membrane wrapping of CNS axons by PI(3,4,5)P3-dependent polarized growth at the inner tongue. *Cell* 156(1-2):277–290.
36. Trapp BD, Quarles RH, Suzuki K (1984) Immunocytochemical studies of quaking mice support a role for the myelin-associated glycoprotein in forming and maintaining the periaxonal space and periaxonal cytoplasmic collar of myelinating Schwann cells. *J Cell Biol* 99(2):594–606.
37. Tait S, et al. (2000) An oligodendrocyte cell adhesion molecule at the site of assembly of the paranodal axo-glial junction. *J Cell Biol* 150(3):657–666.
38. Colavincenzo J, Levine RL (2000) Myelin debris clearance during Wallerian degeneration in the goldfish visual system. *J Neurosci Res* 59(1):47–62.
39. Vaughn JE, Pease DC (1970) Electron microscopic studies of wallerian degeneration in rat optic nerves. II. Astrocytes, oligodendrocytes and adventitial cells. *J Comp Neurol* 140(2):207–226.
40. Chung WS, et al. (2013) Astrocytes mediate synapse elimination through MEGF10 and MERTK pathways. *Nature* 504(7480):394–400.
41. Beisiegel U, Weber W, Ihrke G, Herz J, Stanley KK (1989) The LDL-receptor-related protein, LRP, is an apolipoprotein E-binding protein. *Nature* 341(6238):162–164.
42. Gaultier A, et al. (2009) Low-density lipoprotein receptor-related protein 1 is an essential receptor for myelin phagocytosis. *J Cell Sci* 122(Pt 8):1155–1162.
43. Sun X, et al. (2010) Myelin activates FAK/Akt/NF-kappaB pathways and provokes CR3-dependent inflammatory response in murine system. *PLoS One* 5(2):e9380.
44. Clarner T, et al. (2012) Myelin debris regulates inflammatory responses in an experimental demyelination animal model and multiple sclerosis lesions. *Glia* 60(10): 1468–1480.
45. Xie L, et al. (2013) Sleep drives metabolite clearance from the adult brain. *Science* 342(6156):373–377.
46. Amaya E, Kroll KL (1999) A method for generating transgenic frog embryos. *Methods Mol Biol* 97:393–414.
47. Das B, Brown DD (2004) Controlling transgene expression to study Xenopus laevis metamorphosis. *Proc Natl Acad Sci USA* 101(14):4839–4842.
48. Watson FL, et al. (2012) Cell type-specific translational profiling in the Xenopus laevis retina. *Dev Dyn* 241(12):1960–1972.
49. Kaya F, et al. (2012) Live imaging of targeted cell ablation in Xenopus: A new model to study demyelination and repair. *J Neurosci* 32(37):12885–12895.
50. Pittman AJ, Law MY, Chien CB (2008) Pathfinding in a large vertebrate axon tract: Isotypic interactions guide retinotectal axons at multiple choice points. *Development* 135(17):2865–2871.
51. Nguyen JV, et al. (2011) Myelination transition zone astrocytes are constitutively phagocytic and have synuclein dependent reactivity in glaucoma. *Proc Natl Acad Sci USA* 108(3):1176–1181.
52. Kremer JR, Mastronarde DN, McIntosh JR (1996) Computer visualization of three-dimensional image data using IMOD. *J Struct Biol* 116(1):71–76.
53. Stricker D (2008) BrightStat.com: Free statistics online. *Comput Methods Programs Biomed* 92(1):135–143.
54. Brand M, et al. (1996) Mutations in zebrafish genes affecting the formation of the boundary between midbrain and hindbrain. *Development* 123:179–190.
55. Wang Z, Brown DD (1991) A gene expression screen. *Proc Natl Acad Sci USA* 88(24): 11505–11509.